Dynamic interaction between dislocations and obstacles in bcc iron based on atomic potentials derived using neural networks

Hideki Mori ⬡,[1,*] Tomohito Tsuru ⬡,[2] Masahiko Okumura ⬡,[3] Daisuke Matsunaka ⬡,[4]
Yoshinori Shiihara ⬡,[5] and Mitsuhiro Itakura[3]

[1]*Department of Mechanical Engineering, College of Industrial Technology, 1-27-1 Nishikoya, Amagasaki, Hyogo 661-0047, Japan*
[2]*Nuclear Engineering Research Center, Japan Atomic Energy Agency, Tokai-mura, Ibaraki 319-1195, Japan*
[3]*Center for Computational Science & e-Systems, Japan Atomic Energy Agency, 178-4 Wakashiba, Kashiwa, Chiba 277-0871, Japan*
[4]*Department of Mechanical Systems Engineering, Shinshu University, 4-17-1 Wakasato, Nagano, Nagano 380-8553, Japan*
[5]*Graduate School of Engineering, Toyota Technological Institute, Nagoya, Aichi 468-8511, Japan*

The introduction of obstacles (e.g., precipitates) for controlling dislocation motion in molecular structures is a prevalent method for designing the mechanical strength of metals. Owing to the nanoscale size of the dislocation core ($\leqslant 1$ nm), atomic modeling is required to investigate the interactions between the dislocation and obstacles. However, conventional empirical potentials are not adequately accurate in contrast to calculations based on density functional theory (DFT). Therefore, the atomic-level details of the interactions between the dislocations and obstacles remain unclarified. To this end, in this paper, we applied an artificial neural network (ANN) framework to construct an atomic potential by leveraging the high accuracy of DFT. Using the constructed ANN potential, we investigated the dynamic interaction between the $(a_0/2)\langle 111 \rangle \{110\}$ edge dislocation and obstacles in body-centered cubic (bcc) iron. When the dislocation crossed the void, an ultrasmooth and symmetric half-loop was observed for the bowing-out dislocation. Except for the screw dislocation, the Peierls stress of all the dislocations predicted using the ANN was <100 MPa. More importantly, the results confirmed the formation of an Orowan loop in the interaction between a rigid sphere and dislocation. Furthermore, we discovered a phenomenon in which the Orowan loop disintegrated into two small loops during its interaction with the rigid sphere and dislocation.

I. INTRODUCTION

Enhancing and designing the mechanical strength of metals is vital for building a sustainable society. In principle, the mechanical strength of metals is governed by dislocation dynamics. Accordingly, the introduction of obstacles, e.g., precipitates, is a prevalent approach for controlling the dislocation motion to alter the mechanical strength of metals. Therefore, the investigation of the interaction between dislocations and obstacles forms the starting point for designing the mechanical strength of metals. Owing to the small size of the dislocation core—typically, <1 nm—investigating the interaction between the dislocations and obstacles requires direct treatment of atomic discreetness. Moreover, the long-range elastic interaction of dislocations demands atomic modeling on the scale of 1 000 000 atoms to observe the dynamic interaction between dislocations and obstacles. Therefore, based on the techniques of molecular mechanics (MM) and molecular dynamics (MD), empirical interatomic potentials such as the embedded atom method (EAM) are used for investigating the dynamic interactions between dislocations and obstacles [1–12]. However, the structure and energetics of the dislocation core predicted using empirical interatomic potentials are often inconsistent with the results

of first-principles calculations obtained using density functional theory (DFT) [13]. The existing empirical interatomic potential cannot accurately reproduce the screw-dislocation-core structure and energetics of body-centered cubic (bcc) iron, in contrast to the calculations based on DFT [14,15]. Furthermore, the energetics of M111, referred to as $70.5°$ or $71°$ mixed dislocation in bcc iron, estimated by the empirical interatomic potentials vary significantly from that obtained by DFT calculations [16,17]. When studying the dynamic interactions between dislocations and obstacles, all pure and mixed dislocation components are crucial for the crossing and bypassing mechanism, as this enables dislocations to surpass obstacles. Thus, the precise details of the interaction between the dislocations and obstacles in bcc iron are still obscure.

To this end, we developed an atomic potential using an artificial neural network (ANN) framework with DFT [18–20]. In addition to the screw-dislocation-core structure and its energetics, other mixed-dislocation-core structures and extended lattice defects predicted by the constructed ANN potential were in excellent agreement with those calculated by DFT [18,19]. These results demonstrated the reproducibility and transferability of the constructed ANN potential for investigating dislocation dynamics with DFT. In this paper, we investigate the interaction between edge dislocation and obstacles using the constructed ANN potential by performing 1 000 000 steps of MD simulation with 1 000 000 atoms by the highly accurate ANN potential based on DFT data.
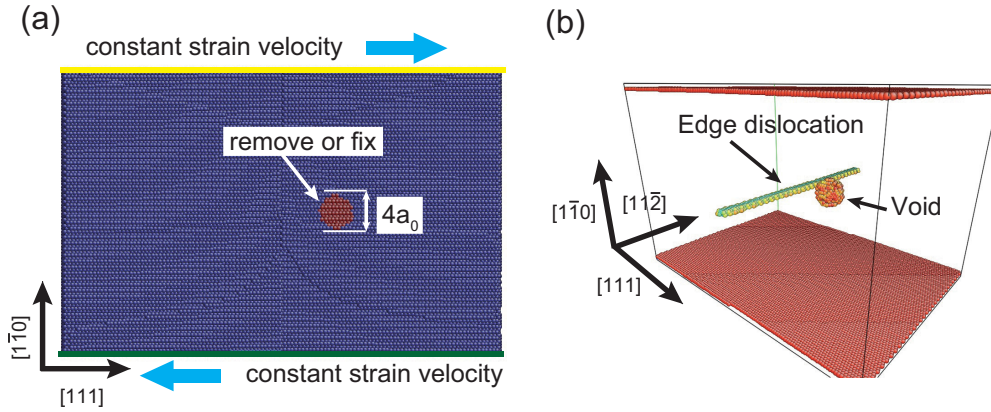
---

*morih@cit.sangitan.ac.jp

FIG. 1. Schematic of atomic model for simulating edge dislocation dynamics, (a) condition of surface layer to yield driving force, and (b) positional relationship between edge dislocation and void in the initial state.

II. COMPUTATIONAL METHODOLOGY

A. Construction and framework of ANN potential

To investigate the dislocation core structure, we constructed an ANN potential based on the ANN method proposed by Behler and Parrinello [21]. In this method, the output of the ANN is the atomic energy $\epsilon_i^{\mathrm{ANN}}$ of the ith atom, and the total energy E^{ANN} of the target system is expressed as the contribution of the atomic energy as follows:

$$E^{\mathrm{ANN}} = \sum_{i=1}^{N} \epsilon_i^{\mathrm{ANN}}[\mathbf{G}(\mathbf{R}_i)], \qquad (1)$$

where N is the number of atoms in a target system; $\mathbf{G}$ is the vector set of descriptors, which describes the local atomic environment around the ith atom; and $\mathbf{R}_i$ represents the atomic positions around the ith atom. We used the Chebyshev descriptors proposed by Artrith *et al.* [22]. The total dimension of the input vector set of descriptors was 20. The Chebyshev descriptors and improvement of cutoff functions are described in Appendix A. We used the swish function as the activation function of the hidden layers in the ANN potential, with 10 neurons in each layer [23]. For training the ANN potential, we used the ÆNET package by Artrith and Urban [24], with the limited-memory Broyden-Fletcher-Goldfarb-Shanno method [25]. The final mean absolute and root mean square errors of the ANN potential for the training dataset were 1.5 and 2.4 meV/atom, respectively. The ANN potential parameter file is stored in our repository as Fe_v03 [26]. The QUANTUM ESPRESSO package [27] was used to construct the reference DFT structure energy datasets for iron. We prepared 6348 atomic structure energy datasets of iron [18]. The number of atoms in the dataset ranges from 1 to 54. All atomic structures and the total energy in the dataset are also freely available online [28].

B. Dislocation dynamics setting

Herein, we investigate the dynamic interaction between $(a_0/2)\langle 111\rangle\{110\}$-edge dislocation and an obstacle in bcc iron, where a_0 denotes the lattice constant of bcc iron. We used the $60[111] \times 48[1\bar{1}0] \times 30[11\bar{2}]$ bcc bulk model, which is periodic along the [111] and $[11\bar{2}]$ directions and contains

a free surface in $[1\bar{1}0]$. To create the edge-dislocation-core structure, we removed the upper-half layer on the (111) plane. Thereafter, we uniformly expanded and contracted the upper- and lower-half blocks by $0.5b$ in the [111] direction, respectively, where b denotes the length of Burger's vector $\frac{\sqrt{3}}{2}a_0$. Simultaneously, the periodic cell length along the [111] direction was contracted by $0.5b$. Subsequently, the atomic position of the model was optimized with constant boundary conditions, and the edge dislocation core was obtained at the center of the $(11\bar{2})$ plane. For the target obstacle, a void was set as a soft limit obstacle, which is vital for a structural material in nuclear fusion systems. To create the void, the atoms in the spherical region were eliminated, and the scale of the sphere was set as $4 \times a_0$, as depicted in Fig. 1(a). In Fig. 1(b), the atomic relationship between the edge dislocation and the void was visualized using the central symmetry parameter function of ATOMEYE [29,30]. Furthermore, the driving force for edge dislocation motion was generated by rigidly moving the upper and lower surface regions in proportion to the strain rate $\dot{\gamma}$, as indicated in Fig. 1(a). Specifically, $\dot{\gamma}$ was set as $10^7\,\mathrm{s}^{-1}$. The applied shear stress τ was evaluated by

$$\tau = \frac{1}{2A_{(110)}}\Big[\sum f_{[111]}^{\mathrm{upper}} - \sum f_{[111]}^{\mathrm{lower}}\Big], \qquad (2)$$

where $A_{(110)}$ denotes the area of the (110) free surface, and $f_{[111]}$ denotes the atomic forces applied to displace the atoms on each surface in the [111] direction [1–3]. We set the time step as 1 fs in the MD simulation. To avoid unexpected rare events for thermal activation, we used a Nosé-Hoover thermostat to maintain the constant temperature 10 K [31,32]. The thermal activation process plays an important role in the mobility of dislocation and interaction between dislocation and obstacle; however, we will study this in the future.

III. RESULTS AND DISCUSSION

A. Interaction between edge dislocation and void

By using the LAMMPS code [33], MD calculations with 500 000 steps were performed with an atomic dislocation model containing 1 032 570 atoms to investigate the dynamics of an edge dislocation interacting with a void. In Fig. 2,
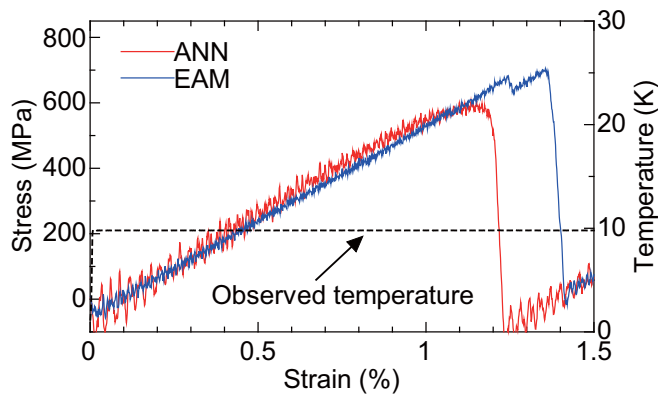
FIG. 2. Stress-strain curve of edge dislocation crossing the void, as predicted by artificial neural network (ANN) and embedded atom method (EAM) [34] potentials. The dashed line is the observed temperature in the molecular dynamics (MD) simulation. Refer to text for detail.

the stress-strain curves are the results of simulating by both ANN and EAM [34] potentials. The ANN and EAM potentials predicted the critical stress of the void, defined as the maximum stress required to cross (bypass) and separate from an obstacle, as 600 and 700 MPa, respectively. Thus, the EAM potential overestimated the critical stress of the edge dislocation by ∼15%. The observed temperature history in the MD simulation using the ANN potential is shown in Fig. 2. In the entire simulation, the temperature of the system was maintained constant at 10 K, which was the target value of the thermostat. This indicates that the effect of thermal activation is small in the present simulation.

However, the atomic detail was observed for all regions between the ANN and EAM potentials. As shown in Fig. 3(a)(i),
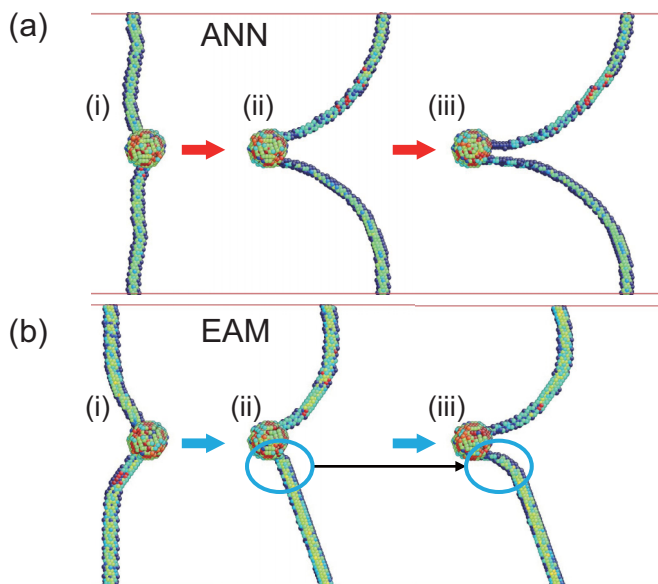

FIG. 3. Schematic of atomic detail of edge dislocation crossing void predicted by (a) the artificial neural network (ANN) potential and (b) embedded atom method (EAM) potential. Roman numerals represent the order of progression of edge dislocation. Refer to text for detail.

in the initial stage of interaction between the edge dislocation and the void, the dislocation line of the ANN potential was highly oscillating [35]. In contrast, the dislocation line of the EAM potential exhibited a stable motion, as shown in Fig. 3(b)(i). Near the critical stress point in the stress-strain curves, a discontinuous variation was observed in the EAM potential, and at this instant, the shape of the dislocation half-loop alternated for bowing out, denoted by the blue circle in Figs. 3(b)(ii)–3(b)(iii). In all simulations of the ANN potential, the dislocation half-loop for bowing out exhibited an ultrasmooth and symmetric shape, as shown in Fig. 3(a) [35]. We emphasize that our simulations of the ANN potential are consistent with experimental observations [36]. In contrast, the dislocation half-loop for bowing out predicted by the EAM potential manifested an asymmetric shape, which can also be seen in Fig. 3(b) [35]. This type of asymmetric shape of the dislocation line during the bowing process has been commonly observed using the EAM potential and has been troubling researchers for many years [1–12]. Thus, the cause of these shape variations during bowing out from the interaction between the dislocation and the void at the atomic level must be determined for both potentials.

B. The Peierls stress of dislocation series

Accordingly, we determined the bowing-out shape of the dislocation based on the mobility of all mixed dislocations, including edge and screw dislocations. Therefore, the variations in mobility between various mixed dislocations can be attributed as a cause of this difference. The Peierls stress is defined as the minimum applied stress required to drive each dislocation at 0 K, which is fundamental for the mobility of several dislocations. Thus, to investigate the origin of the variations observed in this paper, the Peierls stress of the edge, screw, and other mixed dislocations were determined using the ANN and EAM potentials. We selected the six mixed $a_0/2\langle 111\rangle\{110\}$ dislocations, including screw and edge dislocations. The angles of these dislocations were 0°, 35°, 71°, 90°, 125°, and 165°. We defined the angle θ_{mix} of the mixed dislocations using the following relationship between the dislocation line vector $\boldsymbol{\eta}$ and Burger's vector $\mathbf{b}$:

$$\theta_{\text{mix}} = \frac{180}{\pi} \arccos\left(\frac{\boldsymbol{\eta} \cdot \mathbf{b}}{|\boldsymbol{\eta}||\mathbf{b}|}\right). \quad (3)$$

In this definition, $\theta_{\text{mix}} = 0°$ (and $180°$) and $\theta_{\text{mix}} = 90°$ represent screw and edge dislocations, respectively. Except for screw dislocation, all dislocations were generated in a manner almost like the fabrication of edge dislocation as mentioned above. In the case of screw dislocation, no layer was removed, and only its displacement field was added to the initial model. Thereafter, the dislocation core structures were optimized by applying shear force f_a on the free surface along the $\langle 111\rangle$ direction according to the conjugate gradient method. Upon obtaining the optimized dislocation core structure, the applied shear force was step-wise increased. The Peierls stress is defined as the critical stress at failure to optimize the dislocation core structure. The applied shear stress was evaluated as $f_a/A_{\langle 110\rangle}$, as listed in Table I. For reference, the Peierls stresses in bcc iron calculated using the Gaussian approximation potential (GAP) [37–39], which is a high-accuracy

TABLE I. Peierls stress predicted by the ANN potential, EAM [34] potential, and GAP [37–40] in units of MPa.

	0°	35°	71°	90°	125°	165°
ANN	1500	13	79	2.4	47	4.2
EAM	1300	260	1300	85	1000	60
GAP	2000	25	168	14	163	15

machine-learning-based potential model, are presented in Table I. Note that the computational cost incurred by GAP is 157 times that by the ANN potential. Therefore, the MD simulation of dislocation dynamics on the ANN potential scale using GAP is practically impossible. We discuss the computational efficiency of the ANN, EAM potential, and GAP in Appendix B. The Peierls stress of screw dislocation by the ANN potential was 1500 MPa, which is consistent with the DFT results (1000–1650 MPa) [14,15,41,42] as well as the Peierls stresses calculated by the EAM potential (1300 MPa) and GAP (2000 MPa). In contrast, the Peierls stresses of the edge dislocations predicted by the ANN and EAM potentials were 2.4 and 85 MPa, respectively. Compared with the results of the EAM potential, the Peierls stress of the edge by the ANN potential was significantly low. This could be the possible reason causing the broad oscillations of the dislocation line in the initial stage of the simulation by the ANN potential. Furthermore, the Peierls stresses of mixed dislocations exhibited highly distinctive features in both potentials. In all cases, the Peierls stresses of the mixed dislocations obtained using the ANN potential were <100 MPa, which is at least an order smaller than that of screw dislocations. In contrast, the Peierls stresses of edge and other mixed dislocations calculated by the EAM potential ranged from 60 to 1300 MPa. More specifically, the Peierls stress of the 71° mixed dislocation was 1300 MPa, which was almost equal to the Peierls stress of the screw dislocation. The Peierls stresses of edge and other mixed dislocations by GAP were slightly larger than that evaluated by the ANN potential, but its trend of the distribution was consistent with results from the ANN potential. Moreover, the Peierls stress of the 71° mixed dislocation estimated using DFT calculations was ∼10 MPa [16,17], which is consistent with the results obtained using the ANN potential. Experimental observations also indicate that edge and mixed dislocations have higher mobility than screw dislocations [36]. Thus, we can conclude that the Peierls stresses of dislocations in bcc iron are ≲100 MPa, except for screw dislocations. In addition, we concluded that the EAM potential significantly overestimated the Peierls stress of the mixed dislocations [43]. As observed, the EAM potential predicted an asymmetrical shape of the bowing-out dislocation, which can be considered an artificial result caused by the low transferability of the EAM potential. Surprisingly, despite the large differences between the Peierls stresses predicted by the ANN and EAM potentials, the critical stress required to cross the void varied only by 15%. We believe that this phenomenon was influenced by the linear elastic interactions occurring between the dislocations at critical stress. However, we emphasize that the motion and reaction of the dislocations predicted by the ANN potential differed from that of the EAM potential. Overall, these results
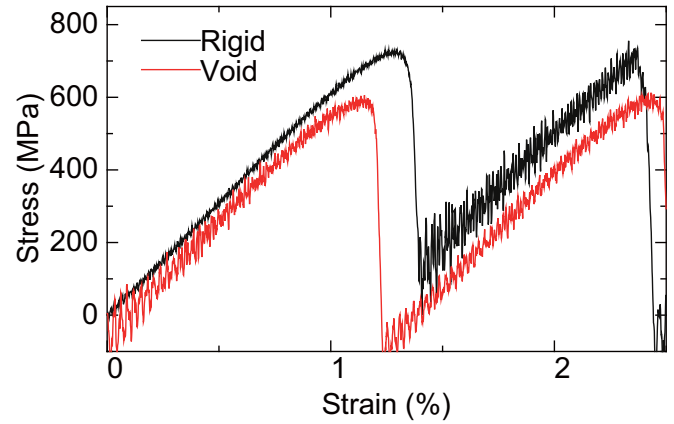

FIG. 4. Stress-strain curve of edge dislocation bypassing rigid sphere predicted using the artificial neural network (ANN) potential compared with the void case.

suggest that more careful investigations of the dislocation dynamics at the atomic level are required to construct the input parameter for such discrete dislocation dynamics. As the Peierls stress of edge dislocation was on the order of a few megapascal, the Peierls barrier was estimated in the sub-meV/b scale [16,17]. At least 100 atoms are required to evaluate the Peierls stress and barrier [16]. Therefore, DFT cannot be used in practice to calculate the potentials at the atomic scale with such accuracy.

C. Interaction between edge dislocation and rigid sphere

The final aim of this paper is to investigate the dynamic interaction between the $(a_0/2)\langle 111\rangle\{110\}$-edge dislocation and the rigid sphere as hard limit obstacles. To create the rigid sphere, the atoms in the spherical region were fixed, and the scale of the sphere was set as $4 \times a_0$, as depicted in Fig. 1(a). We explore the interactions occurring between the dislocation rigid sphere as well as those between the dislocation and the dislocation loop, which remains after the dislocation bypasses the rigid sphere. Accordingly, we performed 1 000 000 steps of MD calculation using a dislocation model with 1 032 570 atoms. Therefore, in this calculation, we performed 1 trillion atomic force evaluations with the accuracy level of DFT, which cannot be achieved with direct DFT calculations. In Fig. 4, the stress-strain curves are the results of a simulation by the ANN potential. The ANN potential predicted that a critical stress of 730 MPa is required to bypass the rigid sphere, which is slightly greater than that of the void. The formation of the Orowan loop around the rigid sphere is depicted in Figs. 5(a)(i) and 5(a)(ii). After bypassing the rigid sphere, the edge dislocation smoothly transited away from the rigid sphere. However, owing to the periodic boundary condition of the migration of the edge dislocation, the edge dislocation would further encounter the rigid sphere. As the Orowan loop prevailed around the rigid sphere at this instant, the interaction between the Orowan loop and the approaching edge dislocation could be investigated. As displayed in Fig. 5, in the initial stage of interactions between the Orowan loop and edge dislocation, the edge dislocation line exhibited broad oscillations. Thereafter, the edge dislocation started
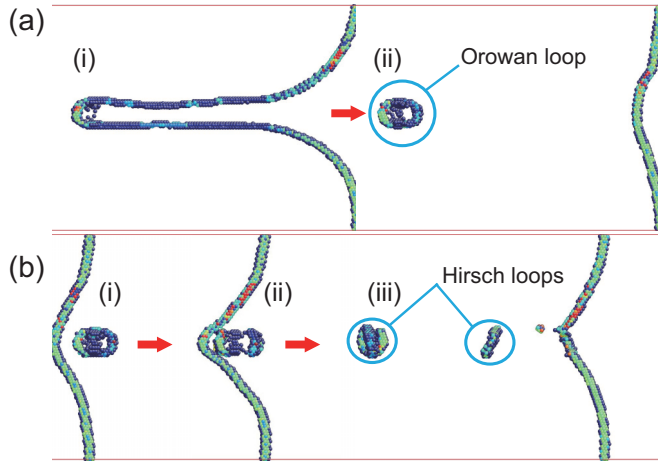
FIG. 5. Schematic of atomic detail of the edge dislocation by-passing the (a) rigid sphere and (b) Orowan loop predicted by the artificial neural network (ANN) potential. Roman numerals represent the order of progression of edge dislocation. Refer to text for detail.

to bow out to bypass the Orowan loop, whereas the screw component of the Orowan loop started to progress toward the repulsive elastic interactions between the edge dislocation and the Orowan loop [35]. Subsequently, the Orowan loop disintegrated into small loops at the front and rear of the rigid sphere. The formation mechanism of these small loops was initially proposed by Hirsch as an alternative to that of the Orowan loop [44,45]. Thus, these small loops are hereinafter referred to as Hirsch loops [44–47]. The critical stress required to bypass the Orowan loop was 730 MPa, which is equal to that required to bypass the rigid sphere. The Hirsch looping mechanism for bypassing the Orowan loop has already been reported for hexagonal close-packed and face-centered cubic metals [46,47]. In this paper, we report the observation of the Hirsch looping mechanism in bcc iron. Furthermore, as stated in the previous studies as well as in this paper, the Hirsch looping in edge dislocation does not occur directly but materializes via Orowan looping [44–47].

IV. CONCLUSIONS

In summary, in this paper, we applied an ANN potential to investigate the dynamic interaction between $(a_0/2)\langle 111 \rangle\{110\}$-edge dislocation and obstacle in bcc iron by leveraging the accurate calculations of DFT. Compared with the asymmetric half-loop obtained with the EAM potential, that obtained with the ANN potential better predicted an ultra-smooth and symmetric half-loop for bowing-out dislocations. In addition, these variations were apparently caused by the significant differences in the Peierls stress between the ANN and EAM potentials. Except for screw dislocation, the Peierls stresses of all the dislocations predicted by the ANN were <100 MPa. The Peierls stress of the edge dislocation was 2.4 MPa. The observations confirmed the formation of an Orowan loop in the interaction between a rigid sphere and an edge dislocation, which later segmented into small loops and displayed a phenomenon that was earlier unknown. These results were observed by leveraging the high accuracy of DFT with the ANN potential. We believe that the obtained data

will be essential for evaluating dislocation dynamics across several scales. Notably, high-accuracy ANN-based atomic potentials have been proposed in various systems composed of single elements as well as alloys and impurities [48–54]. We demonstrate that our constructed ANN potential has the ability to perform dislocation dynamics with high accuracy. By expanding our constructed ANN potential to binary and trinity systems, we will be able to clarify not only the origin of the mechanical strength of bcc metals but also the effect of impurities on bcc metals. In this paper, we only used the standard parallelization method for the CPU of LAMMPS [33]. By combining with the state-of-the-art GPU-acceleration technique [55], the ANN potential will be able to perform large-scale high-throughput calculation with high accuracy. Overall, the atomic potentials derived in this paper using an ANN will aid in advancing material design.

APPENDIX A: DETAIL OF CHEBYSHEV DESCRIPTORS AND THE IMPROVEMENT OF THE CUTOFF FUNCTIONS

In Chebyshev descriptors, the two-body radial contribution is described as

$$G_\alpha^{\text{pair}} = \sum_{j \neq i} T_\alpha \left(\frac{2r_{ij}}{R_c} - 1 \right) f_c(r_{ij}), \tag{A1}$$

where r_{ij} is the atomic distance between atoms i and j, R_c is the cutoff radius, and T_α is the Chebyshev polynomial of the first kind [22]. The Chebyshev polynomials T_n are defined by a recurrence relation as

$$T_{n+1}(x) = 2xT_n(x) - T_{n-1}(x), \tag{A2}$$

where $T_0(x)$ and $T_1(x)$ are 1 and x, respectively. The three-body angle contribution is also described as

$$G_\alpha^{\text{triple}} = \sum_{j \neq i, k \neq i, j} T_\alpha \left[\frac{1}{2} (\cos \theta_{ijk} + 1) \right] f_c(r_{ij}) f_c(r_{ik}), \tag{A3}$$

where r_{ij}, r_{ik}, and r_{jk} are the atomic distances between atoms i, j, and k, and θ_{ijk} is the angle defined by the three atoms [18]. Because of the introduction of the cutoff function $f_c(r_{ij})$, only atoms within the cutoff radius R_c are considered in the sum of Eqs. (A1) and (A3), and the calculation cost remains $O(N)$. Here, f_c is required to smoothly truncate both the value and its first derivative at R_c. In the original version of our ANN potential [18], we used a cosine cutoff function defined as

$$f_c(r_{ij}) = \begin{cases} \frac{1}{2}\left[\cos\left(\frac{\pi r_{ij}}{R_c}\right) + 1\right] & (r_{ij} \leqslant R_c) \\ 0 & (r_{ij} > R_c) \end{cases}, \tag{A4}$$

and set R_c at 0.65 nm in both two- and three-body contributions. The computational cost increases in proportion to the
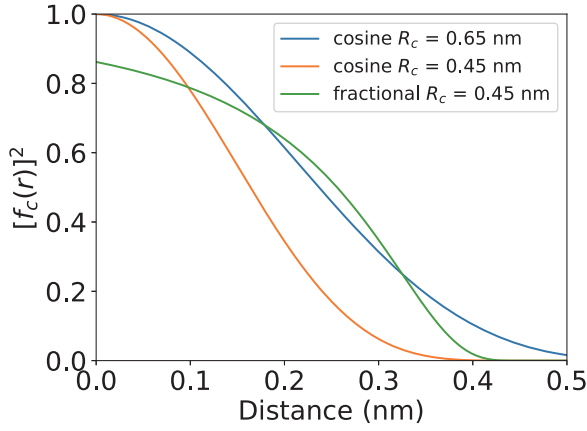
FIG. 6. Change of square of cosine and fractional cutoff function in range of 0.0–0.5 nm.

sixth power of R_c. Therefore, the setting of R_c and formula of f_c play critical roles in the computational efficiency and accuracy of ANN potentials. Especially in the three-body contribution, f_c is multiplied twice. For a change in $r_{ij(ik)}$, the three-body contribution changes in proportion to the square of f_c. As shown in Fig. 6, when R_c is shortened from 0.65 to 0.45 nm, the square of the cosine cutoff function becomes very small in the range of 0.25–0.35 nm. Therefore, the ANN cannot identify the changes in the three-body contribution in this area. To overcome this problem, we used a fractional cutoff function defined as

$$f_c(r_{ij}) = \begin{cases} \frac{X^2}{1+X^2} & (r_{ij} \leqslant R_c) \\ 0 & (r_{ij} > R_c) \end{cases}, \qquad (A5)$$

where X is defined as $X = (r_{ij} - R_c)/h$, and h is set as 0.125 nm [53,56]. As shown in Fig. 6, the fractional cutoff function maintains its value and gradually decreases for distances between 0.25 and 0.35 nm. Therefore, the ANN can identify the changes in the three-body contribution in

TABLE II. Computational times to evaluate the energy and force of one atom on one CPU core of the ANN potential, the previous version of the ANN potential [18], the EAM potential [34], and GAP [37–40].

Units	ANN	EAM	ANN [18]	GAP
μs	103	1.8	2070	16 144
s_{ANN}^{-1}	1	0.017	20	157

this area. For two-body contribution, we used a power cutoff function defined as

$$f_c(r_{ij}) = \begin{cases} 1 + g\left(\frac{r_{ij}}{R_c}\right)^{g+1} - (g+1)\left(\frac{r_{ij}}{R_c}\right)^g & (r_{ij} \leqslant R_c) \\ 0 & (r_{ij} > R_c) \end{cases}, \qquad (A6)$$

where g is set as 3 [57]. We used R_c as 0.55 and 0.45 nm for two- and three-body contributions, respectively. By adopting these cutoff functions, we succeeded in reducing the computational cost while maintaining accuracy [18–20].

APPENDIX B: COMPARISON OF COMPUTATIONAL TIMES FOR EACH POTENTIAL

Table II presents the computational time to evaluate the energy and force of one atom on one CPU core of the ANN potential on an Intel processor (Xeon Gold 6132, 2.6 GHz). For reference, the computational time of the EAM [34], the previous version of the ANN potential [18], and GAP [37–40] are presented in Table II. The computational cost incurred by the ANN potential is 57 times that by the EAM potential. However, the computational time of the ANN potential is 157 times faster than that of GAP. The time spent for our typical simulations, where atomic models include 1 000 000 atoms and a MD step corresponds to 1 000 000 steps, was ∼22 d using the standard parallelization method of the LAMMPS code [33] on 56 CPU cores.

[1] Y. N. Osetsky, D. Bacon, and V. Mohles, Atomic modelling of strengthening mechanisms due to voids and copper precipitates in α-iron, Philos. Mag. **83**, 3623 (2003).

[2] D. J. Bacon, Y. N. Osetsky, and Z. Rong, Computer simulation of reactions between an edge dislocation and glissile self-interstitial clusters in iron, Philos. Mag. **86**, 3921 (2006).

[3] D. Terentyev, L. Malerba, D. Bacon, and Y. N. Osetsky, The effect of temperature and strain rate on the interaction between an edge dislocation and an interstitial dislocation loop in α-iron, J. Phys.: Condens. Matter **19**, 456211 (2007).

[4] S. H. Haghighat, J. Fikar, and R. Schäublin, Effect of interatomic potential on the behavior of dislocation-defect interaction simulation in α-Fe, J. Nucl. Mater. **382**, 147 (2008).

[5] S. Queyreau, J. Marian, M. R. Gilbert, and B. D. Wirth, Edge dislocation mobilities in bcc Fe obtained by molecular dynamics, Phys. Rev. B **84**, 064106 (2011).

[6] G. Bonny, D. Terentyev, and L. Malerba, Interaction of screw and edge dislocations with chromium precipitates in ferritic iron: An atomistic study, J. Nucl. Mater. **416**, 70 (2011).

[7] A. Dutta, M. Bhattacharya, N. Gayathri, G. Das, and P. Barat, The mechanism of climb in dislocation-nanovoid interaction, Acta Mater. **60**, 3789 (2012).

[8] R. Schäublin and S. H. Haghighat, Molecular dynamics study of strengthening by nanometric void and Cr alloying in Fe, J. Nucl. Mater. **442**, S643 (2013).

[9] X. Shi, L. Dupuy, B. Devincre, D. Terentyev, and L. Vincent, Interaction of ⟨100⟩ dislocation loops with dislocations studied by dislocation dynamics in α-iron, J. Nucl. Mater. **460**, 37 (2015).

[10] F. Granberg, D. Terentyev, and K. Nordlund, Interaction of dislocations with carbides in bcc Fe studied by molecular dynamics, J. Nucl. Mater. **460**, 23 (2015).

[11] P. Grammatikopoulos, D. J. Bacon, and Y. N. Osetsky, Simulation of the interaction between an edge dislocation and ⟨111⟩ interstitial dislocation loops in α-iron, Radiat. Eff. Defects Solids **174**, 329 (2019).

[12] Z. Wang, M. Yu, X. Long, C. Yang, N. Gao, Z. Yao, and X. Wang, New mechanisms of dislocation line-loop interactions in

bcc-Fe explored by molecular dynamics method, Resul. Phys. **34**, 105226 (2022).

[13] M. R. Fellinger, A. M. Z. Tan, L. G. Hector, Jr., and D. R. Trinkle, Geometries of edge and mixed dislocations in bcc Fe from first-principles calculations, Phys. Rev. Mater. **2**, 113605 (2018).

[14] M. Itakura, H. Kaburaki, and M. Yamaguchi, First-principles study on the mobility of screw dislocations in bcc iron, Acta Mater. **60**, 3698 (2012).

[15] L. Ventelon, F. Willaime, E. Clouet, and D. Rodney, *ab initio* investigation of the Peierls potential of screw dislocations in bcc Fe and W, Acta Mater. **61**, 3973 (2013).

[16] L. Romaner, T. Pradhan, A. Kholtobina, R. Drautz, and M. Mrovec, Theoretical investigation of the 70.5° mixed dislocations in body-centered cubic transition metals, Acta Mater. **217**, 117154 (2021).

[17] S. Starikov, D. Smirnova, T. Pradhan, Y. Lysogorskiy, H. Chapman, M. Mrovec, and R. Drautz, Angular-dependent interatomic potential for large-scale atomistic simulation of iron: Development and comprehensive comparison with existing interatomic models, Phys. Rev. Mater. **5**, 063607 (2021).

[18] H. Mori and T. Ozaki, Neural network atomic potential to investigate the dislocation dynamics in bcc iron, Phys. Rev. Mater. **4**, 040601(R) (2020).

[19] Y. Shiihara, R. Kanazawa, D. Matsunaka, I. Lobzenko, T. Tsuru, M. Kohyama, and H. Mori, Artificial neural network molecular mechanics of iron grain boundaries, Scr. Mater. **207**, 114268 (2022).

[20] T. Suzudo, K. Ebihara, T. Tsuru, and H. Mori, Cleavages along {110} in bcc iron emit dislocations from the curved crack fronts, Sci. Rep. **12**, 19701 (2022).

[21] J. Behler and M. Parrinello, Generalized Neural-Network Representation of High-Dimensional Potential-Energy Surfaces, Phys. Rev. Lett. **98**, 146401 (2007).

[22] N. Artrith, A. Urban, and G. Ceder, Efficient and accurate machine-learning interpolation of atomic energies in compositions with many species, Phys. Rev. B **96**, 014112 (2017).

[23] P. Ramachandran, B. Zoph, and Q. V. Le, Searching for activation functions, arXiv:1710.05941.

[24] N. Artrith and A. Urban, An implementation of artificial neural-network potentials for atomistic materials simulations: Performance for TiO$_2$, Comput. Mater. Sci. **114**, 135 (2016).

[25] R. H. Byrd, P. Lu, J. Nocedal, and C. Zhu, A limited memory algorithm for bound constrained optimization, SIAM J. Sci. Comput. **16**, 1190 (1995).

[26] https://github.com/HidekiMori-CIT/aenet-lammps.

[27] P. Giannozzi, S. Baroni, N. Bonini, M. Calandra, R. Car, C. Cavazzoni, D. Ceresoli, G. L. Chiarotti, M. Cococcioni, I. Dabo *et al.*, QUANTUM ESPRESSO: A modular and open-source software project for quantum simulations of materials, J. Phys.: Condens. Matter **21**, 395502 (2009).

[28] https://github.com/HidekiMori-CIT/XSF.

[29] C. L. Kelchner, S. J. Plimpton, and J. C. Hamilton, Dislocation nucleation and defect structure during surface indentation, Phys. Rev. B **58**, 11085 (1998).

[30] J. Li, AtomEye: An efficient atomistic configuration viewer, Modelling Simul. Mater. Sci. Eng. **11**, 173 (2003).

[31] S. Nosé, A unified formulation of the constant temperature molecular dynamics methods, J. Chem. Phys. **81**, 511 (1984).

[32] W. G. Hoover, Canonical dynamics: Equilibrium phase-space distributions, Phys. Rev. A **31**, 1695 (1985).

[33] A. P. Thompson, H. M. Aktulga, R. Berger, D. S. Bolintineanu, W. M. Brown, P. S. Crozier, P. J. in't Veld, A. Kohlmeyer, S. G. Moore, T. D. Nguyen *et al.*, LAMMPS—A flexible simulation tool for particle-based materials modeling at the atomic, meso, and continuum scales, Comput. Phys. Commun. **271**, 108171 (2022).

[34] M. Mendelev, S. Han, D. Srolovitz, G. Ackland, D. Sun, and M. Asta, Development of new interatomic potentials appropriate for crystalline and liquid iron, Philos. Mag. **83**, 3977 (2003).

[35] See Supplemental Material at http://link.aps.org/supplemental/10.1103/PhysRevMaterials.7.063605 for animations of the whole simulation of the interaction between dislocation and obstacles predicted by the ANN potential and the EAM potential in Figs. 3(a), 3(b), and 5.

[36] D. Caillard, Kinetics of dislocations in pure Fe. Part I. *in situ* straining experiments at room temperature, Acta Mater. **58**, 3493 (2010).

[37] A. P. Bartók, M. C. Payne, R. Kondor, and G. Csányi, Gaussian Approximation Potentials: The Accuracy of Quantum Mechanics, without the Electrons, Phys. Rev. Lett. **104**, 136403 (2010).

[38] A. P. Bartók, R. Kondor, and G. Csányi, On representing chemical environments, Phys. Rev. B **87**, 184115 (2013).

[39] D. Dragoni, T. D. Daff, G. Csányi, and N. Marzari, Achieving dft accuracy with a machine-learning interatomic potential: Thermomechanics and defects in bcc ferromagnetic iron, Phys. Rev. Mater. **2**, 013808 (2018).

[40] G. Csányi, S. Winfield, J. R. Kermode, A. De Vita, A. Comisso, N. Bernstein, and M. C. Payne, Expressive programming for computational physics in Fortran 950+, IoP Comput. Phys. Newsletter, (2007).

[41] L. Dezerald, L. Proville, L. Ventelon, F. Willaime, and D. Rodney, First-principles prediction of kink-pair activation enthalpy on screw dislocations in bcc transition metals: V, Nb, Ta, Mo, W, and Fe, Phys. Rev. B **91**, 094105 (2015).

[42] B. Bienvenu, L. Dezerald, D. Rodney, and E. Clouet, *ab initio* informed yield criterion across body-centered cubic transition metals, Acta Mater. **236**, 118098 (2022).

[43] K. Kang, V. V. Bulatov, and W. Cai, Singular orientations and faceted motion of dislocations in body-centered cubic crystals, Proc. Natl. Acad. Sci. USA **109**, 15174 (2012).

[44] F. Humphreys and P. B. Hirsch, The deformation of single crystals of copper and copper-zinc alloys containing alumina particles—II. Microstructure and dislocation-particle interactions, Proc. R. Soc. Lond. A **318**, 73 (1970).

[45] T. Hatano, Dynamics of a dislocation bypassing an impenetrable precipitate: The Hirsch mechanism revisited, Phys. Rev. B **74**, 020102(R) (2006).

[46] S. Groh, Transformation of shear loop into prismatic loops during bypass of an array of impenetrable particles by edge dislocations, Mater. Sci. Eng. A **618**, 29 (2014).

[47] S. Xu, D. L. McDowell, and I. J. Beyerlein, Sequential obstacle interactions with dislocations in a planar array, Acta Mater. **174**, 160 (2019).

[48] F.-S. Meng, J.-P. Du, S. Shinzato, H. Mori, P. Yu, K. Matsubara, N. Ishikawa, and S. Ogata, General-purpose neural network interatomic potential for the α-iron and hydrogen binary system:

Toward atomic-scale understanding of hydrogen embrittlement, Phys. Rev. Mater. **5**, 113606 (2021).

[49] H. Kimizuka, B. Thomsen, and M. Shiga, Artificial neural network-based path integral simulations of hydrogen isotope diffusion in palladium, J. Phys. Energy **4**, 034004 (2022).

[50] M. Ohbitsu, T. Yokoi, Y. Noda, E. Kamiyama, T. Ushiro, H. Nagakura, K. Sueoka, and K. Matsunaga, Atomic structures and stability of finite-size extended interstitial defects in silicon: Large-scale molecular simulations with a neural-network potential, Scr. Mater. **214**, 114650 (2022).

[51] T. Yokoi, K. Adachi, S. Iwase, and K. Matsunaga, Accurate prediction of grain boundary structures and energetics in CdTe: A machine-learning potential approach, Phys. Chem. Chem. Phys. **24**, 1620 (2022).

[52] R. Freitas and Y. Cao, Machine-learning potentials for crystal defects, MRS Commun. **12**, 510 (2022).

[53] I. Lobzenko, Y. Shiihara, H. Mori, and T. Tsuru, Influence of group IV element on basic mechanical properties of bcc medium-entropy alloys using machine-learning potentials, Comput. Mater. Sci. **219**, 112010 (2023).

[54] M. S. Nitol, K. Dang, S. J. Fensin, M. I. Baskes, D. E. Dickel, and C. D. Barrett, Hybrid interatomic potential for Sn, Phys. Rev. Mater. **7**, 043601 (2023).

[55] M. Zhang, K. Hibi, and J. Inoue, GPU-accelerated artificial neural network potential for molecular dynamics simulation, Comput. Phys. Commun. **285**, 108655 (2023).

[56] Y. Mishin, D. Farkas, M. Mehl, and D. Papaconstantopoulos, Interatomic potentials for monoatomic metals from experimental data and *ab initio* calculations, Phys. Rev. B **59**, 3393 (1999).

[57] A. Khorshidi and A. A. Peterson, Amp: A modular approach to machine learning in atomistic simulations, Comput. Phys. Commun. **207**, 310 (2016).